



Universiteit Utrecht

BACHELOR THESIS

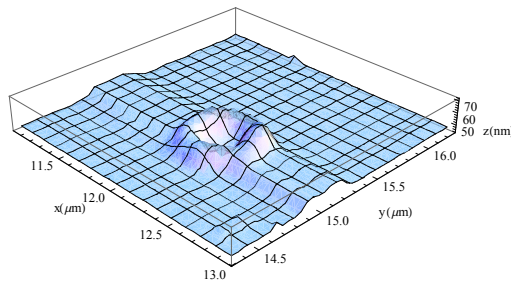
Single-shot ablation of silicon-on-insulator by femtosecond violet laser pulses

Author:

Joris KATTEMÖLLE

Supervisor:

Dr. D van OOSTEN



DEBYE INSTITUTE FOR NANOMATERIALS SCIENCE
June 21, 2013

Contents

1	Introduction	2
2	Theory	2
2.1	Ablation	2
2.2	Second Harmonic Generation	5
2.2.1	Introduction	5
2.2.2	Linear versus Nonlinear media	5
2.2.3	The source term	6
2.2.4	Intensity of the generated electrical field	8
2.2.5	Phase matching	9
3	Experimental setup	12
3.1	Overview	12
3.2	The incident laser beam	13
3.2.1	Before entering the objective	14
3.2.2	At the focal plane	16
3.3	The lens diameter	17
3.4	The (movement of) the sample	17
3.5	Focussing	17
3.6	Measurement of the pulse energy	18
3.7	Some remarks about the use of optical components designed for 800 nm	19
4	Results	20
4.1	The two created arrays	20
4.2	Morphologies	20
4.3	Crater depth versus pulse energy	23
5	Discussion and Conclusion	23

1 Introduction

Why shoot holes in silicon-on-insulator, using a laser? First of all, the way in which light interacts with matter is of great fundamental interest. As of yet, not much is understood about this interaction on small time and length scales, and research in laser ablation could shed more light on these processes.

Secondly, silicon is a basic material for many devices and ablation is a tool for micromachining this material with high precision. Learning more about - and enhancing - this tool will increase the possibilities in silicon manipulation, which could prove to play an important role in the development and enhancement of new technology.

For very precise manipulation, one wants to be able to make very small holes. So far, it has been demonstrated by Zhang *et al.* [23] that for infrared wavelength ($\lambda = 800 \text{ nm}$), holes with a diameter of around $0.6 \mu\text{m}$ can be ablated.

As far as we know, ablation with a 400 nm wavelength has not yet been performed. Therefore, the question remains whether or not this shorter wavelength reduces the hole size. On the one hand the shorter wavelength can be focused better. On the other hand, it is a process much more linear, as is discussed in the theory section (2.1).

In this thesis, we set out to determine an upper limit to the smallest hole size achievable using a wavelength of 400 nm , and make an estimation of the fluence at which this occurs.

2 Theory

2.1 Ablation

Generally speaking, ablation is a process in which material is locally removed. We speak of laser ablation, when this removal is induced by an incident laser beam. For short laser pulses the ablation process is separated into three temporal regions [17], which are presented in the following three paragraphs.

Excitation The process of excitation, or absorption of the pulse energy, takes place in the time domain of the pulse duration ($\sim 100 \text{ fs}$) [17]. For semiconductors such as silicon this means that electrons in the valence band are promoted to the conduction band by one- or two-photon absorption. This absorption takes place only when the one- or two-photon energy is enough to cross the band gap. The rate at which these carriers are created can be

written as [20]

$$\frac{\partial N(z, t)}{\partial t} = [\alpha_0 + \frac{1}{2}\beta I(z, t)] \frac{I(z, t)}{\hbar\omega}, \quad (1)$$

where $N(z, t)$ is the amount of free carriers at depth z and time t , α_0 and β the one- and two photon absorption coefficients (abbreviated OPA coefficient and TPA coefficient respectively), and finally $I(z, t)$ the local pump intensity.

We see that in the case of infra-red light¹ interacting with silicon, where $\alpha_0 = 1021 \text{ cm}^{-1}$ [8] and $\beta = 1.85 \text{ GW cm}^{-1}$ [4], the term proportional to $\beta I^2(z, t)$ dominates for high intensities. In this case therefore, free carrier generation will be a very nonlinear process.

When we compare this to the corresponding OPA coefficient for violet light² $\alpha_0 = 9.52 \times 10^4 \text{ cm}^{-1}$ [9] we see immediately that it is greater by about two orders of magnitude. The two-photon absorption coefficient, on the other hand, will be of the same order of magnitude.³ The free carrier generation at these wavelengths is therefore a much more linear process as opposed to infra-red wavelength induced free carrier generation.

Solving the first order free carrier differential equation (1) is not as easy as it might appear due to the non-trivial $I(z, t)$. For high pulse energies, the beginning of the pulse already creates a dense electron plasma, which in turn locally affects the properties of the material; in particular the interaction of light with the material. For example, photons can scatter from the induced plasma, and the dielectric constant becomes more metal-like because of the free electrons. The rest of the pulse arrives at the material altered by that same pulse and will, for example, be more reflected because of the higher dielectric constant. It can get even more complex when the incoming light consists out of a wide range of k-vectors, which is so in the case of focusing by an objective with a high Numerical Aperture (N.A.). Because the reflectivity changes during the arrival of the pulse, it a challenge to correctly predict the amount that is reflected, the so-called *self-reflectivity*. These processes can, however, be correctly modelled by Finite Difference Time Domain (FDTD) methods, as is done by H. Zhang [22].

¹Here specifically, light with a wavelength of 800 nm.

²Here specifically, the wavelength we have used for ablation; $\lambda = 400 \text{ nm}$.

³For wavelengths this short, the TPA coefficients are not tabulated anymore. We *assume* that the TPA coefficient for violet wavelengths is equal or less compared to the TPA coefficient for infra-red wavelengths because in the latter case, two photons already have enough energy to easily cross the band gap. This is, of course, even more the case for photons with higher energy. For a two-photon energy of 4.6 eV, *i.e.* a wavelength of 540 nm, we did find a TPA coefficient of $\beta = 0.3 \text{ GW cm}^{-1}$ [16], giving us more confidence in the assumption.

Melting After the electrons are excited by the pulse they couple to phonons, *i.e.* they transfer their energy to the lattice. This is a process that takes place in the second time domain, which is roughly from one to ten picoseconds [17].

Usually the *two-temperature* model is then applied [5,6,22]. It considers, not surprisingly, two temperatures, being the electron temperature T_e and the lattice temperature T_l . The way in which these temperatures affect each other is governed by two coupled differential equations which relate the rate of change of the energy density and the Laplacian of the temperature to the intensity and temperature *difference* between the two systems for both the electrons and the lattice.

A satisfactory treatment of this subject is out of the scope of this discussion. We therefore would like to refer you to the aforementioned references [5,6,22] for examples of the application of the two-temperature model, or to reference [19] for an overview.

Expansion and Ablation The last time domain is that of expansion and/or ablation, and takes place in the order of 100 ps to 1 ns [17]. It is the slowest process because unlike the two previous processes, the lattice atoms need to be moved in order for the material to deform, and they are relatively heavy. The criterion that is set for the material not just to deform, but also to eject, greatly varies amongst various authors.

Some use the criterion of *evaporation enthalpy* [6]; when due to the total temperature the enthalpy exceeds the enthalpy for evaporation, material is sublimated.

Others use a *fluence* criterion [22]. The local fluence can be obtained by integrating the local intensity over the duration of the pulse. When this local fluence exceeds the peak fluence at the damage threshold, *i.e.* the minimal pulse energy for which ablation is observed, the point is part of the region that is to be the crater.

Still others use the *mean square bonding length fluctuation* [13]

$$\delta(t) = \frac{2}{N(N-1)} \sum_{\substack{i,j \\ i>j}} \frac{\sqrt{\langle r_{ij}(t)^2 \rangle - \langle r_{ij}(t) \rangle^2}}{\langle r_{ij}(t) \rangle}, \quad (2)$$

which is a more statistical approach. The brackets $\langle \rangle$ define the mean value over a Molecular Dynamics (MD) simulation time interval. $\delta(t)$ is essentially the normalized sum over the uncertainty in the inter-particle distance. When the lattice remains unchanged because of a low pulse energy, $\delta(t)$ will not change much. For the liquid (melted) state however, the inter-atomic dis-

tances $r_{i,j}$ keep changing, which is reflected by a higher $\delta(t)$. An even higher $\delta(t)$ occurs when atoms, or bunches of atoms, leave the sample.

Conclusion In this subsection, we have seen that the process of femtosecond laser ablation can be separated into three temporal regimes: Excitation, Melting, and Expansion/Ablation. In each regime theoretical and experimental progress still remains to be made in order to fully understand the underlying processes. Not surprisingly therefore, it is a very active field of research.

2.2 Second Harmonic Generation

2.2.1 Introduction

Not every frequency of laser light is directly accessible due to a limited amount of usable gain media and optical transitions. A valuable way of increasing the number of accessible frequencies is the use of nonlinear effects in certain anisotropic media. Here we discuss the electrodynamic fundamentals of this process, and see how this helps the second harmonic generation (SHG).

Specifically, we use these effects in our experiment in order to have $\lambda = 400$ nm laser pulses at our disposal. We do this using a β -Barium-Borate (BBO) crystal, as can be read in section 3.

2.2.2 Linear versus Nonlinear media

In elementary electrodynamics one usually only considers the so called Linear Isotropic Homogeneous (LIH) media, where, amongst other things, there is a linear relation between the polarization of the medium (\mathbf{P}) and the applied electric field (\mathbf{E}) [11]:

$$\mathbf{P} = \varepsilon_0 \chi \mathbf{E}.$$

Here ε_0 is the electric constant and χ the electric susceptibility. In isotropic materials there will be no term proportional to \mathbf{E}^2 . One can easily understand why this has to be so.

Assume, on the contrary, that the material is isotropic, and that there is a term proportional to \mathbf{E}^2 . Say \mathbf{E} points in the ‘up’ direction, producing a polarization \mathbf{P} . We now rotate the field by π to get $-\mathbf{E}$. The polarization will not be $-\mathbf{P}$ due to the quadratic term, in contradiction with the assumption that the material is isotropic.

Not all materials are isotropic, of course. A more general statement for the polarization therefore includes higher-order terms of the electric field [3]

$$\mathbf{P} = \varepsilon_0 \chi^{(1)} \mathbf{E} + \varepsilon_0 \chi^{(2)} \mathbf{E}^2 + \varepsilon_0 \chi^{(3)} \mathbf{E}^3 + \dots$$

Here $\chi^{(i)}$ is the electric susceptibility for the i 'th power of \mathbf{E} . Note that in this case they are *tensors*⁴. In anisotropic media \mathbf{P} and \mathbf{E} need not to point in the same direction.

2.2.3 The source term

Let's see what happens when a material has the property

$$\mathbf{P} = \varepsilon_0\chi^{(1)}\mathbf{E} + \varepsilon_0\chi^{(2)}\mathbf{E}^2. \quad (3)$$

Hereto, we first derive the wave equation for electromagnetic waves inside the material as induced by Maxwell's equations.

Firstly,

$$\begin{aligned} \mathbf{D} &\equiv \varepsilon_0\mathbf{E} + \mathbf{P} \\ &= \varepsilon_0\mathbf{E} + (\varepsilon_0\chi^{(1)}\mathbf{E} + \varepsilon_0\chi^{(2)}\mathbf{E}^2) \\ &= \varepsilon_0(1 + \chi^{(1)})\mathbf{E} + \varepsilon_0\chi^{(2)}\mathbf{E}^2 \\ &= \varepsilon\mathbf{E} + \varepsilon_0\chi^{(2)}\mathbf{E}^2, \end{aligned} \quad (4)$$

where $\varepsilon \equiv \varepsilon_0\varepsilon_r$ and ε_r the relative dielectric constant.

Secondly,

$$\nabla \times \mathbf{H} = \mathbf{J}_f + \frac{\partial \mathbf{D}}{\partial t}. \quad (5)$$

We now assume the medium to be loss-less, non-magnetic ($\mu = \mu_0$), dielectric ($\mathbf{J}_f = 0$), and ε to be time-independent. This will be a good approximation for the materials and intensities we are interested in. Using equations 3, 4 and 5 we can then write

$$\nabla \times \mathbf{H} = \varepsilon \frac{\partial \mathbf{E}}{\partial t} + \varepsilon_0\chi^{(2)} \frac{\partial \mathbf{E}^2}{\partial t}.$$

With the assumptions made, the $\nabla \times \mathbf{E}$ equation becomes

$$\nabla \times \mathbf{E} = -\frac{\partial \mathbf{B}}{\partial t} = -\mu_0 \frac{\partial \mathbf{H}}{\partial t},$$

where μ_0 is the vacuum permeability. Taking the curl on both sides, we find

$$\nabla \times (\nabla \times \mathbf{E}) = -\mu_0 \frac{\partial}{\partial t} \left\{ \varepsilon \frac{\partial \mathbf{E}}{\partial t} + \varepsilon_0\chi^{(2)} \frac{\partial \mathbf{E}^2}{\partial t} \right\}. \quad (6)$$

⁴Therefore it would possibly be more clear to write $P^j = \varepsilon_0\chi_{jk}^{(1)}E^k + \varepsilon_0\chi_{jkl}^{(2)}E^kE^l + \dots$; here summation is implied over repeated indices. However, the way we have written it in the text is more suggestive, and it is also the way in which one usually finds it in the literature.

By the standard rule for curls $\nabla \times (\nabla \times \mathbf{E}) = \nabla(\nabla \cdot \mathbf{E}) - \nabla^2 \mathbf{E}$, and neglecting the first term because of the absence of free charges, the left hand side becomes $-\nabla^2 \mathbf{E}$. Rearranging terms we then from (6) acquire the *wave equation for dielectrics where the polarization has a quadratic dependence on the electric field*;

$$\boxed{\nabla^2 \mathbf{E} - \mu_0 \varepsilon \frac{\partial^2 \mathbf{E}}{\partial t^2} = \mu_0 \varepsilon_0 \chi^{(2)} \frac{\partial^2 \mathbf{E}^2}{\partial t^2}} \quad (7)$$

Whereas the familiar electromagnetic wave equation reads

$$\nabla^2 \mathbf{E} - \mu_0 \varepsilon \frac{\partial^2 \mathbf{E}}{\partial t^2} = 0.$$

Hence we can see the term that is proportional to $\chi^{(2)} \frac{\partial^2 \mathbf{E}^2}{\partial t^2}$ as a *source term*. As the waves enter the material, the source term enters the equation. We will now calculate this term.⁵

Consider now a plain electromagnetic wave⁶

$$\mathbf{E}_1 = \frac{1}{2} \mathbf{E}_{0,1} e^{i(\omega_1 t - \mathbf{k}_1 \cdot \mathbf{r})} + \text{c.c.} \quad (8)$$

Hence

$$\begin{aligned} \mathbf{E}_1^2 &= \frac{1}{4} \mathbf{E}_{0,1} \mathbf{E}_{0,1}^* e^{2i(\omega_1 t - \mathbf{k}_1 \cdot \mathbf{r})} + \text{c.c} \\ &\quad + \frac{1}{2} |\mathbf{E}_{0,1}|^2. \end{aligned} \quad (9)$$

⁵This can be a little confusing. We do not calculate a solution of the wave equation (7), but rather the ‘contribution’ of the source term to the waves as they would have been without this term.

⁶Note that we have to write *real* fields in order to do this correctly, which is done by adding the complex conjugate (c.c). A very important difference in working with linear versus nonlinear optics, is that we can have squares of the electric field in the latter. In the former one just writes the complex electric field, makes calculations without worrying about the fact that these fields are not complex, and then take the real part in the end. However, if you would do this in nonlinear optics, things can go terribly wrong. Let for example

$$\mathbf{E} = \text{Re} \{ \mathbf{E}_0 e^{i\omega t} \} = \mathbf{E}_0 \cos(\omega t).$$

Then

$$\mathbf{E}^2 \neq \text{Re} \{ (\mathbf{E}_0 e^{i\omega t})^2 \} = E_0^2 \cos(2\omega t),$$

but rather

$$E^2 = (\text{Re} \{ \mathbf{E}_0 e^{i\omega t} \})^2 = E_0^2 \cos^2(\omega t).$$

This is an important result because we see a factor $e^{i2\omega t}$ in the source term. This is exactly why a wave of double the frequency is generated. The $|\mathbf{E}_{0,1}|^2$ term is constant in time and will therefore not influence the system⁷ because in the wave equation (7), there is only the time derivative of $|\mathbf{E}_{0,1}|^2$. With (9) we can calculate the source term as

$$\mu_0 \varepsilon_0 \chi^{(2)} \frac{\partial^2 \mathbf{E}^2}{\partial t^2} = \frac{1}{4} \mu_0 \varepsilon_0 \chi^{(2)} \frac{\partial^2}{\partial t^2} (\mathbf{E}_0 \mathbf{E}_0^* e^{2i(\omega_1 t - \mathbf{k}_1 \cdot \mathbf{r})} + \text{c.c.}).$$

2.2.4 Intensity of the generated electrical field

The question that still remains is what the intensity of the generated field is after passing a distance l through the crystal. For the sake of brevity and simplicity a complete derivation will not be presented here. For a complete treatment of the subject we would like to redirect you to standard books on nonlinear optics.⁸ Merely some key points will be mentioned and commented on.

First, one can define

$$\begin{aligned} \mathbf{E}_2 e^{i(\omega_2 t - \mathbf{k}_3 \cdot \mathbf{r})} &\equiv \chi^{(2)} \mathbf{E}_1^2 e^{2i(\mathbf{k}_2 \cdot \mathbf{r})}, \\ d_{\text{eff}} \mathbf{E}_{0,1}^2 &\equiv \frac{1}{2} \chi_{3jk}^{(2)} E_{0,1}^j E_{0,1}^k, \end{aligned} \quad (10)$$

and

$$\Delta k \equiv 2k_1 - k_2,$$

called the *phase mismatch*.

When (10) is inserted into the wave equation (7) several equations are obtained, including the following one that describes the growth of E_2 with respect to l where l is a vector in the \mathbf{k}_2 direction. [12]

$$\frac{dE_2}{dl} = \frac{i\omega_2^2 d_{\text{eff}} \mathbf{E}_{0,1}^2}{2k_2 c^2} e^{i\Delta k l}. \quad (11)$$

We can get an expression for the amplitude of the generated field at the end of the crystal, $\mathbf{E}_{0,2}(L)$, by integrating equation (11). If we furthermore use that $I(2\omega) = \frac{1}{2} n(2\omega) \varepsilon_0 c |\mathbf{E}_{0,2}(L)|^2$ and $I(\omega) = \frac{1}{2} n(\omega) \varepsilon_0 c |\mathbf{E}_{0,1}|^2$, where $n(\omega)$ is the frequency dependent refractive index and c the speed of light, the intensity of the generated field becomes

$$I(2\omega) = \frac{2\omega^2 d_{\text{eff}}^2 I^2(\omega) L^2}{n(2\omega) n^2(\omega) c^3 \varepsilon_0} \left(\frac{\sin(\Delta k L/2)}{\Delta k L/2} \right)^2. \quad (12)$$

⁷However, for really intense fields this gives rise to a process called *optical rectification* [18]. Frequencies in the THz range will be generated.

⁸See for example *The Principles of Nonlinear Optics* by Y. R. Shen. [2]

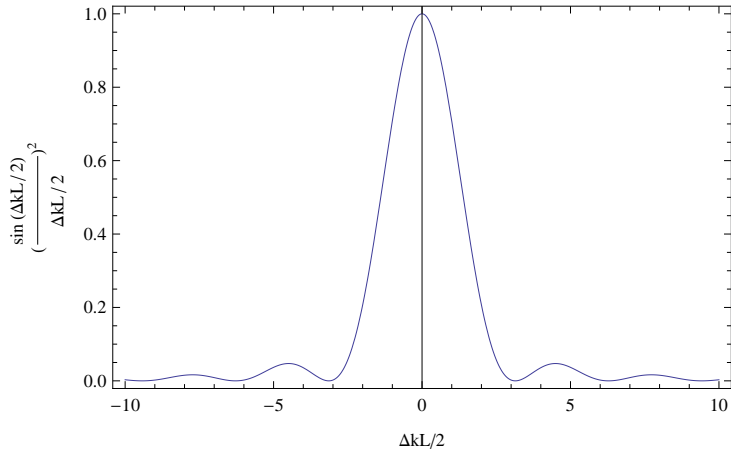


Figure 1: The effect of the *phase mismatch* Δk . The intensity of the generated second harmonic is proportional to the factor on the vertical axis.

2.2.5 Phase matching

As we can see in figure 1, the second harmonic generation is strong only when $\Delta kL/2$ is close to zero. For maximum output, we therefore want the phase mismatch $\Delta k = 2k_1 - k_2$ to be zero, which in terms of the refractive indices is equivalent to

$$\begin{aligned} 2\frac{\omega_1 n(\omega_1)}{c} - \frac{\omega_2 n(\omega_2)}{c} &= 2\frac{\omega n(\omega)}{c} - \frac{2\omega n(2\omega)}{c} = 0 \\ \Rightarrow n(\omega) - n(2\omega) &= 0, \end{aligned} \quad (13)$$

which is also known as the *Second Harmonic Generation phase matching condition*.

For materials with normal dispersion $n(2\omega) > n(\omega)$, and phase matching is not possible. Second Harmonic Generation (SHG) is, however, possible using BBO, because it is birefringent.

BBO is a negative uniaxial crystal, which means that one out of the three crystal axes has a lower refractive index than the other two. This axis is referred to as the extraordinary or optical axis, which we will henceforth refer to as the z axis. The other two are called the ordinary axes, and we will call them the x and y axes. The refractive indices are referred to as n_o for the x and y axes, and n_e for the z axis.

Because of this asymmetry an unpolarized beam entering the crystal will split into two beams, referred to as the extraordinary and ordinary waves. For the former, the \mathbf{E} field lies *in* the yz plane. For the latter the \mathbf{E} field is *perpendicular* to this plane. Consider now the yz plane.

Because the dielectric constant is only different in the direction of the z axis, and the o-wave does not have a z component, it does not feel any different dielectric constant. Hence, for the o-wave, the refractive index is equal for every direction in the xy plane. The e-wave however, has a component of the \mathbf{E} field oscillating in the direction of the z axis, and hence will feel the extraordinary dielectric constant. This component is dependent on the angle to the z axis. Hence is the refractive index for the e-wave a function of this angle. This function is defined by the *index ellipsoid* [15]

$$\frac{y^2}{n_e^2} + \frac{z^2}{n_o^2} = 1.$$

The distance from the origin to a point on this ellipsoid equals the refractive index for the e-wave in that direction. For the o-wave this is a circle (distance n_o in every direction).

The crux is that *the ellipsoid for the refractive index of the e-wave at 2ω , and the circle for the refractive index of the o-wave at ω intersect somewhere. This means that the phase matching condition is satisfied in that direction.*

We plotted these two curves for BBO in the specific case of SHG of 800 nm. (figure 2), using the Sellmeier equations ([14])

$$\begin{aligned} n_o^2(\lambda) &= 2.7405 + \frac{0.0184}{\lambda^2 - 0.0179} - 0.0155\lambda^2 \\ n_e^2(\lambda) &= 2.3730 + \frac{0.0128}{\lambda^2 - 0.0156} - 0.0044\lambda^2, \end{aligned}$$

with λ in μm and in vacuum.

The angle for which the phase matching condition is satisfied, *i.e* the angle for which $n_e(2\omega, \theta) = n_o(\omega)$, where θ is the angle to the z axis, can be found by solving

$$\frac{y_0^2}{n_e^2(2\omega)} + \frac{z_0^2}{n_o^2(2\omega)} = \frac{y_0^2}{n_o^2(\omega)} + \frac{z_0^2}{n_o^2(\omega)} = 1$$

for y_0 and z_0 , and then using $\theta_{\text{pm}} = \arctan(y_0/z_0)$.

In this way we calculated the phase matching angle for SHG of $\lambda = 800$ nm light (thus producing $\lambda = 400$ nm light) to be

$$\theta_{\text{pm}} \simeq 29^\circ.$$

Usually these crystals are cut in such a way, that at an incidence normal to the crystal surface, the beam is at an angle $90^\circ - \theta_{\text{pm}}$ to the crystal axes. Indeed; when we look at the product information of the crystal we used, we find that the faces are cut at an angle $\theta = 29.2^\circ$ [7].

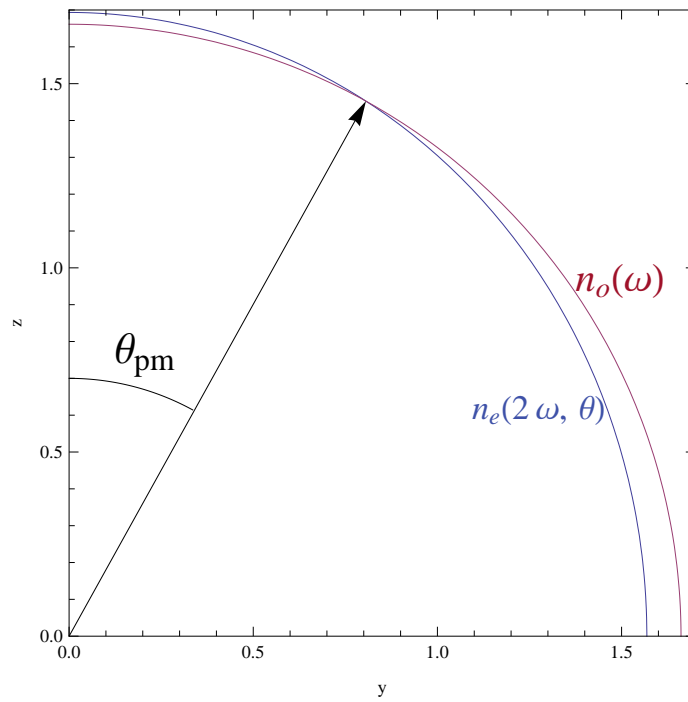


Figure 2: The two relevant refractive indices as a function of θ . z is the extraordinary- and y an ordinary axis. For this plot we used $\omega = c2\pi/800$ nm, and calculated $\theta_{\text{pm}} \simeq 29^\circ$.

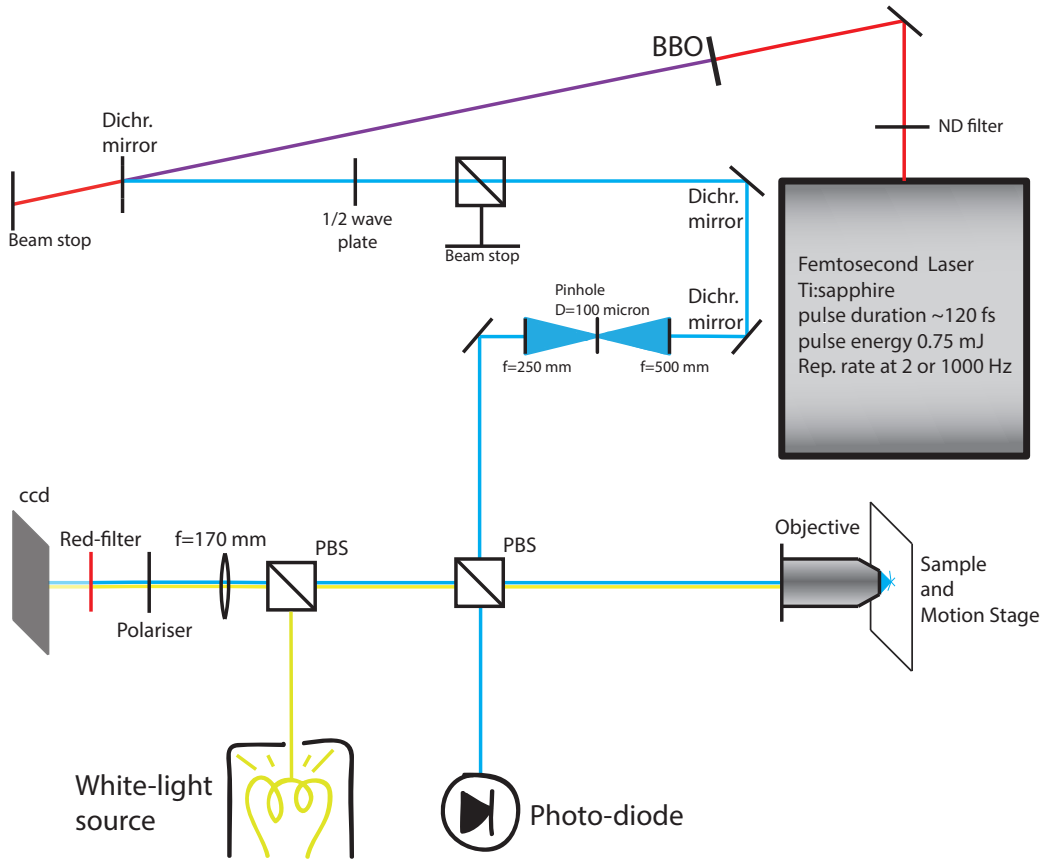


Figure 3: A schematic representation of the setup.

3 Experimental setup

3.1 Overview

The Hurricane laser (Spectra Physics inc.), set to a repetition rate of 1 kHz or 2 Hz, produces pulses with a duration of around 120 fs and an energy of 0.75 mJ. The wavelength is centered around 800 nm, and the $1/e^2$ beam diameter is 6 mm [21]. After the intensity is reduced by filters to about 25%, the pulses pass a thin β -Barium-Borate (BBO) crystal, where second harmonic generation (SHG) takes place and a wavelength of 400 nm is produced.⁹ After the crystal, there is still a lot of residue 800 nm left. This is filtered out by a dichroic mirror, which has a high transmittance for 800 nm, and a high reflectivity for 400 nm. The angle of incidence is chosen as close to 0° as possible for maximal effect.

⁹See the corresponding section (2.2) for more about this process.

The power is then regulated by the composition of a rotatable $\lambda/2$ plate and a polarizing beam splitter (PBS). After two dichromatic mirrors which further enhance the spectral purity, we reach a 1:2 telescope with a spatial filter placed at the focal point.¹⁰

We then arrive at the central beam splitter. One branch goes directly through the microscope objective (Nikon CFI60, $f = 2$ mm), N.A=0.8) and onto the sample. Here, ablation will take place whenever the fluence is above the damage threshold. We move the sample in between shots by a 3-dimensional stepper motor motion stage (Zaber Technologies T-LSM025A). The other branch leads to a photo-diode which measures the (relative) energy per pulse.

In addition to this, we have the possibility to image the sample as well as the beam. For imaging, we use white light to illuminate the sample. The *scattered* light will go back through the objective, the two beam splitters, an imaging lens, a polarizer and a red-filter to finally reach a CCD¹¹ (Qimaging RETIGA 1300). The lens is obviously there to get the image focused on the CCD. The red-filter and polarizer are there to filter out the light coming from the sample. This is necessary to eliminate unwanted reflections on various optical components, originating from the white-light source.

To image the beam one has to remove the red-filter and turn the white-light source off.

Care is taken that the focal plane of the imaging system coincides with the focus of the laser beam. This is done by first finding the focus of the beam, as is explained in section 3.5, and then moving the camera in the longitudinal direction to retain imaging focus. Now, we can find the beam focus better, because we see better when the beam is in focus. Therefore the process is iterated until satisfactory coincidence of imaging- and beam focal plane is achieved.

3.2 The incident laser beam

Clearly, it is of primary experimental interest what is ablated with. So, we measured the beam properties as they are before entering the objective. Sequentially, we discuss the beam properties as they are in the focal plane, where the ablation process will take place. A more complete treatment would also include information about the temporal shape of the pulses, which is excluded here.

¹⁰The filter, amongst other components such as beam splitters and lenses, was designed for the use of 800 nm. In the subsection “Some remarks about the use of optical components designed for 800 nm” (3.7) the possible issues are discussed.

¹¹Charge-coupled device

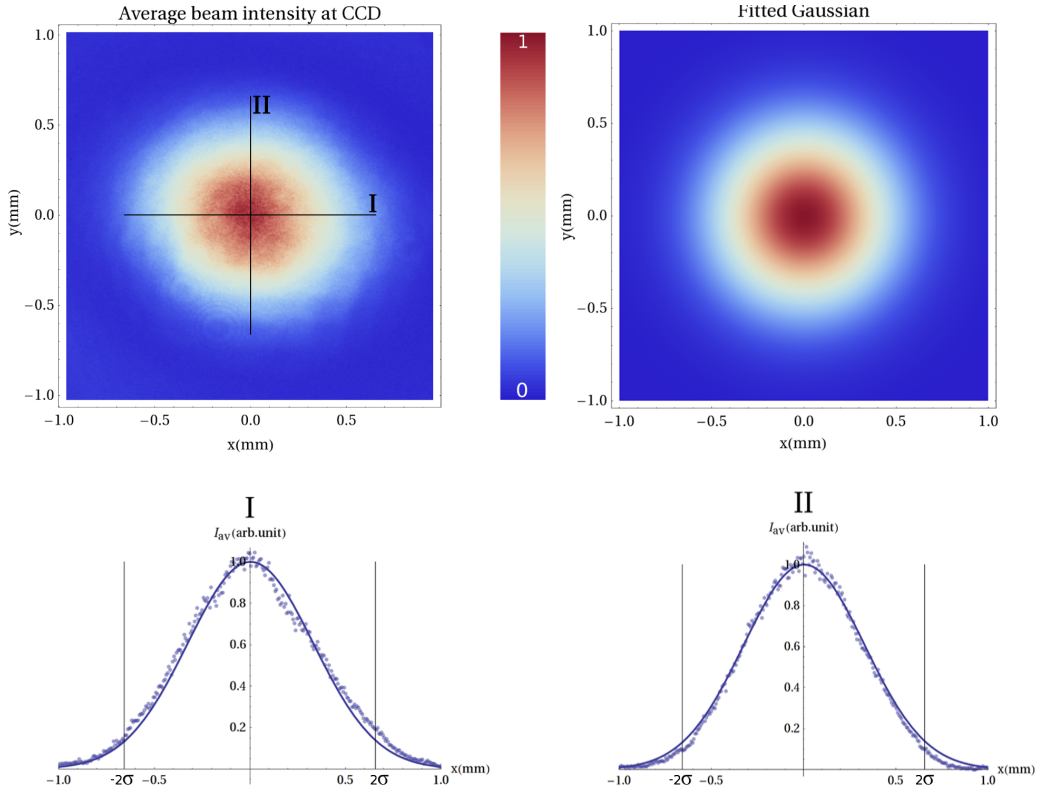


Figure 4: The measured beam profile and its two-dimensional Gaussian fit. For such a Gaussian the $1/e^2$ diameter is equal to four times the standard deviation; $d_0 = 4\sigma \simeq (1.31 \pm 0.05)$ mm. The anisotropy is likely due to a non-perfect perpendicular incidence on the CCD, and is included by the error bars.

3.2.1 Before entering the objective

The beam profile prior to focusing was acquired by removing the objective and putting a CCD instead. It is the same CCD as is used for imaging, but then at a different position.¹² The repetition rate of the laser was set to 1 kHz. The $1/e^2$ beam diameter was determined to be $d_0 = (13.1 \pm 0.05)$ mm by a two-dimensional Gaussian fit to the thus acquired data. These, as well as the fit, are presented in figure 4.

Also, we need to be sure of the spectrum. These results are presented in figures 5 and 6.

¹²To be precise, the CCD was put ~ 15 cm further down the beam because of spatial limitations. We assume the divergence of the beam small enough to be able to neglect the change in diameter over this distance.

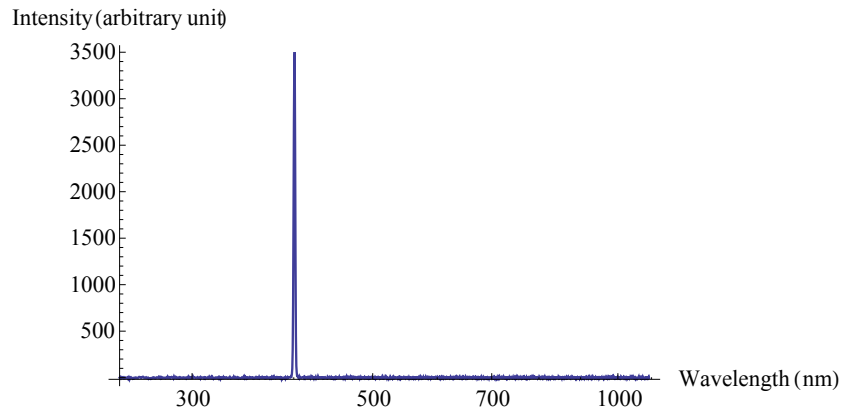


Figure 5: The broadband spectrum. Note that there is no significant increase at $\lambda = 800$ nm.

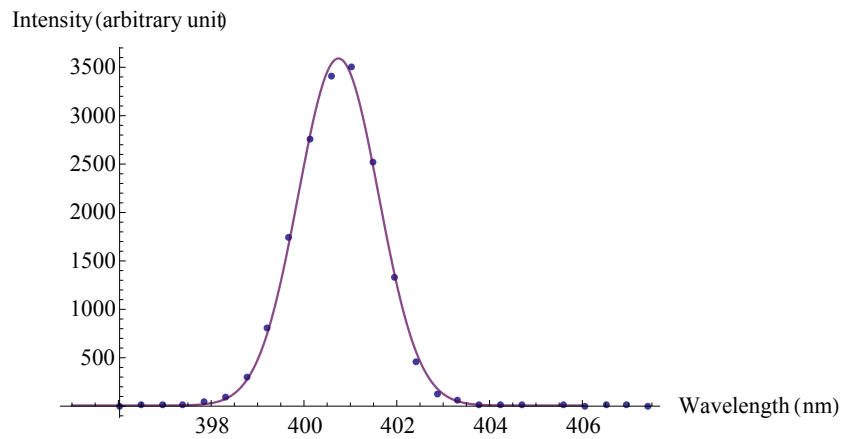


Figure 6: The spectrum is approximately Gaussian. The fitted curve is centered around $\lambda \simeq 400.74$ and has standard deviation of $\sigma \simeq 0.87$.

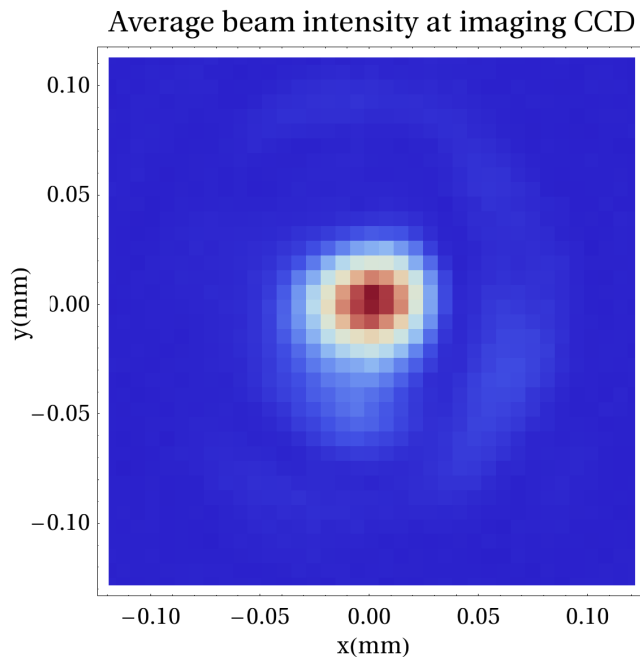


Figure 7: Profile of the beam reflected by the sample, and in focus with the imaging CCD. It is the most isotropic focus shape that is currently practically achievable in our setup. Although an Airy ring can be distinguished, the profile follows a Gaussian one to a good approximation. The calculated $1/e^2$ diameter is $d_{f,\text{CCD}} = (46.84 \pm 0.05) \mu\text{m}$. The (normalized) colour scale is equal to the one in figure 4.

3.2.2 At the focal plane

Because of the short duration and high intensity of the pulses, and the high N.A. we use, simple relations for the focal spot size like $D \sim \lambda/\text{N.A}$ do not apply anymore [22]. We can however obtain an estimate in the following way.

The CCD at its normal position (fig. 3) captures a white light image of the sample. If an array of craters is imaged, we can compare this to the later obtained Atomic Force Microscope (AFM) data of the same array, and thereby easily calculate a magnification factor for the imaging system. Because the laser beam and the white light image are simultaneously in focus (section 3.5), we can also apply this factor to the focal beam diameter of the reflected beam at the CCD. This diameter is obtained by, again, making a Gaussian fit to the captured data, as was also done for the unfocused beam. The data are displayed in figure 7.

Following this procedure, we calculated a magnification factor of $m =$

95.7 ± 4 and a $1/e^2$ focal spot diameter of $d_{f,\text{CCD}} = (46.84 \pm 0.05) \mu\text{m}$ at the CCD, yielding an focal spot diameter of $d_f = d_{f,\text{CCD}}/m = (667.8 \pm 0.3) \text{ nm}$ at the sample. In the determination of the error bars, we assume this is the right way to calculate the focal spot diameter.

3.3 The lens diameter

To our inconvenience, Nikon does not list the lens diameter. We can however calculate it using the N.A. and focal distance.

The numerical aperture is defined as $\text{NA} = n \sin \theta$, where n is the refractive index of the medium in which the lens is supposed to work, and θ the divergence of the focussed beam [10]. For Gaussian beams, the divergence is defined as the angle between the optical axis and the cone of points where the intensity dropped to $1/e^2$. Because of the geometry of the focussing system, this angle equals $\theta = \tan^{-1}(\frac{1}{2}D/f)$ when the beam that enters has no divergence. So, $\text{NA} = \sin[\tan^{-1}(\frac{D}{2f})]$ for use in air, where $n \approx 1$. Thus, $\arcsin[\arctan(\text{NA})] = \frac{D}{2f}$. Using $f = 2 \text{ mm}$ and $\text{NA} = 0.8$ we reach a (calculated) lens diameter of $D = 3 \text{ mm}$.

3.4 The (movement of) the sample

The sample consists out of a thin layer ($\sim 200 \text{ nm}$) of crystalline silicon on top of a $1 \mu\text{m}$ thick layer of silica (SiO_2), which in turn is atop of a Silicon substrate; an composition which goes under the name of *silicon-on-insulator* (SOI).

During an experimental run, the laser is set to a repetition rate of 2 Hz. A computer script is triggered by the laser to move the stage after each shot to ensure every pulse hits a fresh spot. In a meander-like fashion an array of ablated areas is made. During the course of the creation of this array, the per-shot energy is gradually decreased by rotating the $\lambda/2$ plate. The thus achieved pulse energy range is in the order of one- to zero nanojoule. The damage threshold energy is contained in this range.

3.5 Focussing

We find the focus by empirical means. Whilst the laser is set to a repetition rate of 1 kHz we move the sample in longitudinal direction through the point of approximate focus. At a certain point, damage starts to occur after which the stage is halted. We then reduce the pulse energy by rotating the $\lambda/2$ plate. This process is repeated until no damage occurs at any point. We

then know that the previous pulse energy was the threshold energy. At this per-pulse energy then, the focus can be find best.

How good is this method? To find this out we again put the per-pulse energy close to the threshold value. The stage is moved in small steps not only in the longitudinal direction, but also in a transversal direction. Because we can dictate the amount by which the stage moves, we know the longitudinal step size: $\Delta z = 0.5 \mu\text{m}$. We saw that six consecutive holes were created. Thus, if we move the stage until we see damage for the first time, and then $3 \times 0.5 \mu\text{m}$ more, we know we have found the focus within an accuracy of approximately $1 \mu\text{m}$, which is also the focal depth of the objective.

3.6 Measurement of the pulse energy

The pulse energy is measured for each pulse separately. The amplified output voltage of the photo-diode is measured with an oscilloscope (Tektronix 1001B) set to *peak-detect mode*, allowing it to detect glitches as short 10 ns [1]. For every sample, it outputs the maximal and minimal voltage that occurred in the time domain of that sample. We made sure only one pulse arrives in the course of one sample.

Calibration of the photo-diode The photo-diode needs to be calibrated. To do so, we removed the objective, put the laser at a repetition rate of 1 kHz, and measured the average power with a calibrated power meter (Newport 818-SL). By comparing the average power with the photo-diode peak data, we can calculate the relation between the measured peak-voltage per pulse and its energy. In general, the total energy E_{tot} over a time Δt is

$$E_{\text{tot}} = P\Delta t \quad (14)$$

for the power P measured by the power meter. On the other hand, we have for the photo-diode

$$E_{\text{tot}} = \sum_i f(v_i),$$

where i runs over all the pulses that have arrived in time Δt . Assuming the relation f is linear,

$$E_{\text{tot}} = \sum_i (cv_i + v_0) = c \sum_i v_i + Nv_0 = N(c \langle v \rangle + v_0) = \nu \Delta t (c \langle v \rangle + v_0) \quad (15)$$

with c and v_0 the calibration constants, N the amount of pulses in time Δt , $\langle v \rangle$ the voltage over the N pulses, and ν the repetition rate of the laser. By

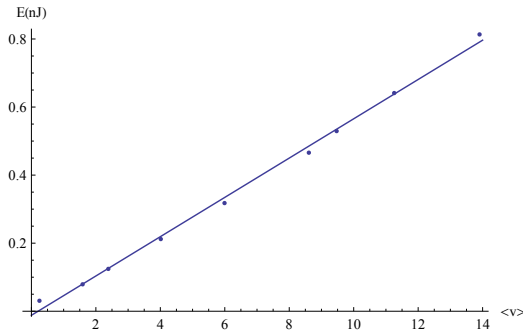


Figure 8: Data and fit used to calibrate the photo diode.

equating (14) and (15) we get

$$c \langle v \rangle + v_0 = \frac{P}{\nu} = E. \quad (16)$$

In figure 8 we plotted the measured data. From a fit the calibration constants c and v_0 are obtained. The relation between the voltage and pulse energy (in nJ) becomes

$$f(v) = 0.0577 - 0.0119v. \quad (17)$$

3.7 Some remarks about the use of optical components designed for 800 nm

Problems emerge because the setup was initially built for the use of 800 nm.

First of all, a lot of intensity is lost due to the anti-reflection coating of various optical components. However, this does not pose a real problem, because albeit these losses enough intensity is able to reach the sample.

Secondly, because the coatings greatly favour the transmittance of 800 nm over that of 400 nm, we could have a substantial amount of residue 800 nm once we reach the sample. By measurement, which is presented in figure 5, we know this is not the case.

Thirdly, the spatial filter is 'too big'¹³. By the rule of thumb determining the appropriate hole size, the diameter to use is linearly dependent on the wavelength. Hence our pinhole is two times 'too big'. This effect is, ironically, compensated for by the fact that the lenses in the telescope have a chromatic aberration. Because of this the beam waist does not coincide with the pinhole. Hence is the pinhole slightly overfilled and some spatial filtering

¹³What 'too big' exactly means depends on the amount of spatial filtering one desires to have.

will still take place. Again intensity is lost, but there still remains enough for the damage threshold to be exceeded. For an idea of the transversal intensity homogeneousness, we profiled the beam as it is before entering the microscope objective (figure 4).

4 Results

4.1 The two created arrays

Two arrays were created. They were scanned using an AFM in tapping mode. The data can be seen in figures 9 and 10. To distinguish between the various craters we define $I_{i,j}$ as the crater in the i 'th row (counted from below) and the j 'th column of the first array. For the second array we use II .

4.2 Morphologies

As was the case for ablation with 800 nm we also see the formation of nanotips; *e.g.* $I_{4,8}$, gentle ablation; *e.g.* $I_{4,7}$, and heavy ablation; *e.g.* $II_{10,2}$. However, the two last morphologies are not nicely separated in terms of their pulse energies. Even at the highest pulse energies that we used for ablation, smooth craters can be seen. A nice example of this is $I_{9,1}$, of which we also show a cross-section (figure 11)

In general, we can say more rim-like structures are observed in comparison with the experiments done by H. Zhang. An example of a typical high-rim structure is shown in figure 12. For some craters even, the local minimum lies above the silicon surface level.

We also see the formation of very small holes, like $II_{6,8}$. It has a diameter of around 200 nm, and a depth of 2.8 nm. A cross-section can be seen in figure 13.

A noteworthy feature is the formation of a bulge at $I_{1,10}$. Initially, it was not meant to be an experimental spot. It was made to function as a marker. First, it received multiple shots of around the same energy as the holes to its left. Then, for a couple of seconds, it received shots at a repetition rate of 1 kHz. Surprisingly, the hole that was likely to be there after the first shot did not get deeper because of more shots. On the contrary; it formed into a bulge.

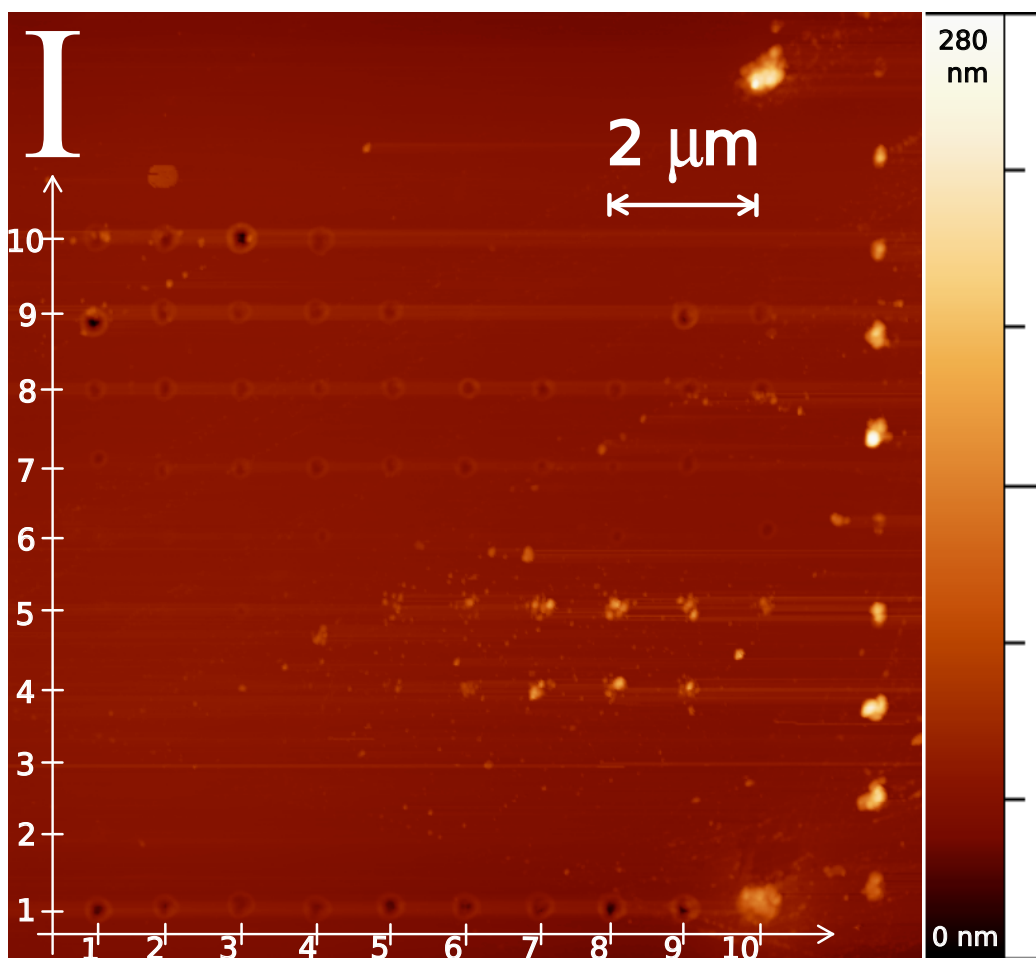


Figure 9: The first array.

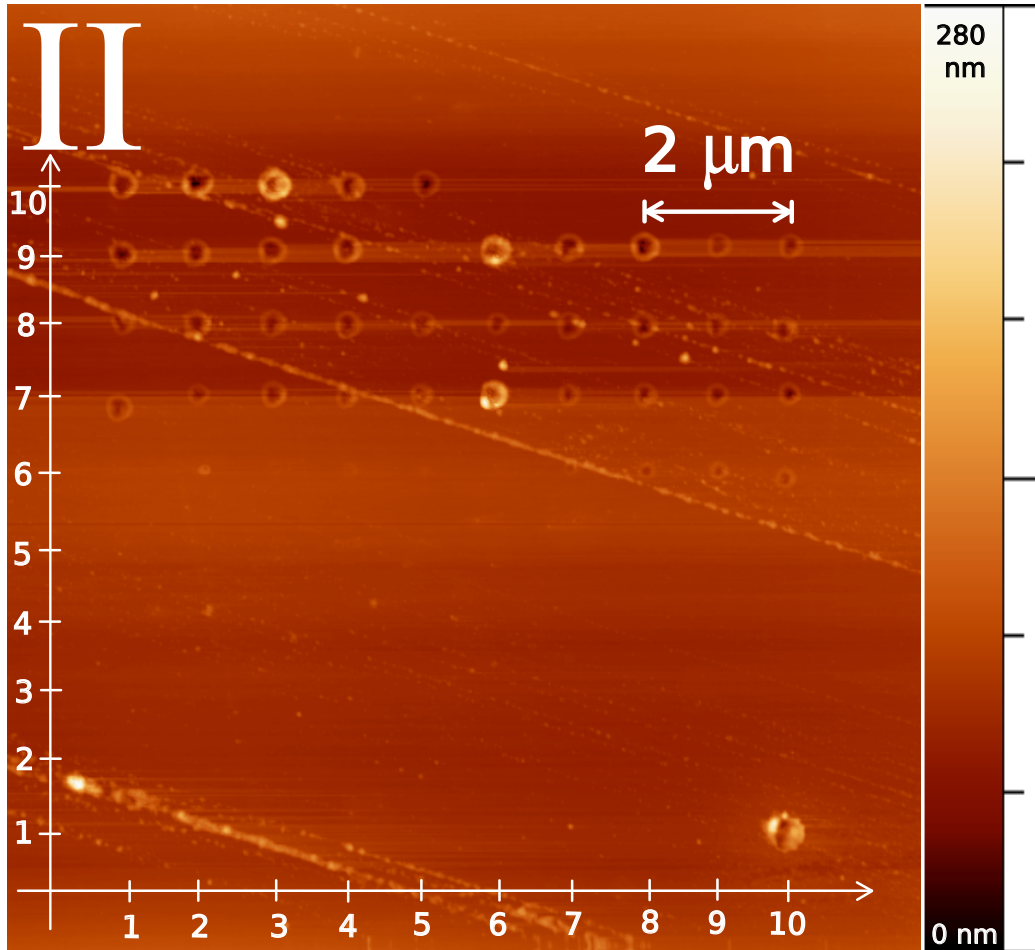


Figure 10: The second array.

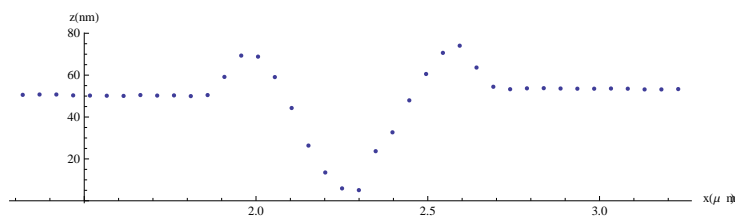


Figure 11: Crater $I_{9,1}$.

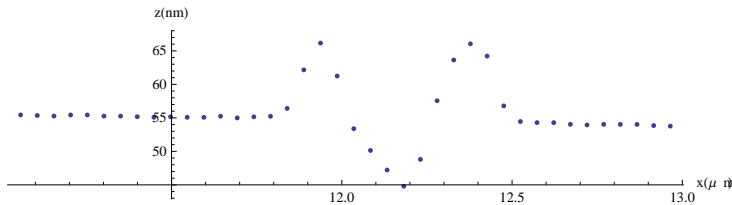


Figure 12: Crater $I_{8,6}$.

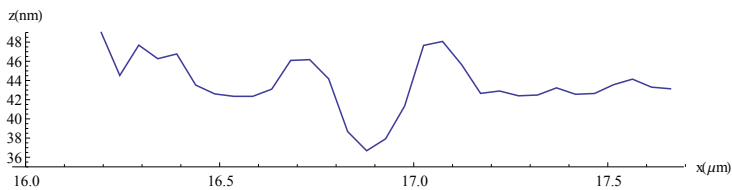


Figure 13: Crater $I_{6,8}$.

4.3 Crater depth versus pulse energy

As will be discussed in the discussion section, our setup was not precise enough for the measurements to be very reproducible. Therefore, we cannot give a precise damage threshold. We can however, give a very rough estimate. We found that, for our craters, the Rim-to-bottom depth was a more sensible parameter than the surface-to-bottom depth. This is because of a greater variation in the latter for equal pulse energies. In figure 14 we present the data. From the graph, we can see that the relation between pulse energy and depth is roughly linear. This is not so for 800 nm light, where first saturation of the depth occurs before reaching the linear regime [22]. By the intersection of this linear relation with the energy axis, we determine the threshold for damage to be 0.5 nJ. Because this is an estimation, we can not yet be precise on the error bars.

Using the beam diameter that was calculated in section 3.2.2, $E = 0.5 \text{ nJ}$ corresponds to a fluence of $F_{\text{thr},400\text{nm}} = 0.5 \text{ nJ} / (\pi(\frac{1}{2}668 \text{ nm})^2) \approx 0.14 \text{ Jcm}^{-2}$, which is slightly more than half the ablation threshold for light at 800 nm: $F_{\text{thr},800\text{nm}} = 0.22 \text{ Jcm}^{-2}$ [13, 22].

5 Discussion and Conclusion

Discussion The three major shortcomings of our experiment are the instability of focus, the photo-diode calibration, and a lack of knowledge about the precise beam properties at the focal spot.

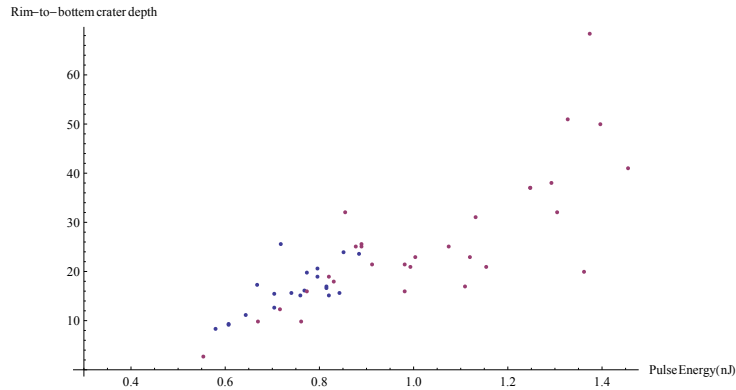


Figure 14: The pulse energy versus the rim-to-bottom depth. The blue points are acquired from array I, the purple ones from array II.

Instability of focus The mount in which the microscope objective is screwed stands on a very high post (18.5 cm). This is too unstable when micrometer precision is demanded. Secondly, also the motion stage is unstable. Each time it moves, it can shake afterwards by as much as $40 \mu\text{m}$. We know this because when the laser was set at 1 kHz and full power, and the stage was moved by a little, damage occurred at places where the stage supposedly never was. Simple solutions to these problems include mounting the objective more securely, and using a two dimensional stage.

Photo-diode calibration Unfortunately, the laser was suddenly very unstable at the time of calibration. Usually the pulse-to-pulse variation is around 1%. Now, the power was oscillating between a peak value and zero over the course of 6 pulses. We lost some low energy pulses in the noise of the photo-diode. However, the power-meter takes the energy of any pulse, how low it may be.

Underfilling The beam has a diameter of 1.3 mm before it enters the objective (section 3.2), and the lens diameter is 3 mm (section 3.3). The fact that light of a smaller wavelength can be focused better could be exploited more by over- instead of underfilling the objective's back aperture.

Conclusion In this thesis, we have seen that the amount of obtainable laser wavelengths can be enlarged with the use of nonlinear effects in certain anisotropic materials. We have used such a material, *i.e.* β -barium borate, to obtain a wavelength of 400 nm. With this wavelength, we ablated silicon-on-insulator and observed the formation of nanotips and craters. Because of

experimental shortcomings we could not yet determine a precise relation between the crater depth and fluence. We have however shown, that ablation using 400 nm light is perfectly possible, that the damage threshold is approximately 0.14 Jcm^{-2} , and that craters with a diameter of at least 200 nm can be formed. Further research remains to be done in order to gain more precision.

References

- [1] *Manual of the TDS1001B*.
- [2] R. W. Boyd. *The Principles of Nonlinear Optics*. Wiley-Interscience, 2003.
- [3] R. W. Boyd. *Nonlinear Optics*. Elsevier, 2008.
- [4] Alan D. Bristow, Nir Rotenberg, and Henry M. van Driel. Two-photon absorption and kerr coefficients of silicon for 850–2200 nm. *Applied Physics Letters*, 90(19):191104, 2007.
- [5] Tae Y. Choi and Costas P. Grigoropoulos. Plasma and ablation dynamics in ultrafast laser processing of crystalline silicon. *Journal of Applied Physics*, 92(9):4918–4925, 2002.
- [6] B.H. Christensen, K. Vestentoft, and P. Balling. Short-pulse ablation rates and the two-temperature model. *Applied Surface Science*, 253(15):6347 – 6352, 2007.
- [7] Eksma. The manufacturer’s website, <http://eksmaoptics.com/femtoline-components/femtoline-nonlinear-laser-crystals/thin-bbo-crystals-for-shg-of-ti-sapphire-laser-wavelength/>, June 2013.
- [8] Eugene G. Gamaly, Saulius Juodkasis, Koichi Nishimura, Hiroaki Misawa, Barry Luther-Davies, Ludovic Hallo, Philippe Nicolai, and Vladimir T. Tikhonchuk. Laser-matter interaction in the bulk of a transparent solid: Confined microexplosion and void formation. *Phys. Rev. B*, 73:214101, Jun 2006.
- [9] Martin A. Green and Mark J. Keevers. Optical properties of intrinsic silicon at 300 k. *Progress in Photovoltaics: Research and Applications*, 3(3):189–192, 1995.
- [10] J. E. Greivenkamp. *Field Guide to Geometrical Optics*. SPIE Optical Engineering Press, 2004.
- [11] J. Griffiths. *Introduction to Electrodynamics*. Pearson Education (US), 2012.
- [12] S. Hooker and C. Webb. *Laser Physics*. Oxford University Press, 2010.

- [13] Harald O. Jeschke, Martin E. Garcia, Matthias Lenzner, Jörn Bonse, Jörg Krüger, and Wolfgang Kautek. Laser ablation thresholds of silicon for different pulse durations: theory and experiment. *Applied Surface Science*, 197198(0):839 – 844, 2002.
- [14] McGraw and Hill. *Handbook of Optics*. McGraw Hill Professional, 3'th edition, 2009.
- [15] P. Piot. From a lecture on the subject given at northern illinois university, http://nicadd.niu.edu/~piot/phys_630/Lesson14.pdf.
- [16] D. H. Reitze, T. R. Zhang, Wm. M. Wood, and M. C. Downer. *J. Opt. Soc. Am. B*.
- [17] B. Rethfeld, K. Sokolowski-Tinten, D. von der Linde, and S.I. Anisimov. Timescales in the response of materials to femtosecond laser excitation. *Applied Physics A*, 79(4-6):767–769, 2004.
- [18] W. T. Silfvast. *Laser Fundamentals*. Cambridge University Press, 2004.
- [19] N. Singh. Two-Temperature Model of non-equilibrium electron relaxation: A Review. *eprint arXiv:cond-mat/0702331*, feb 2007.
- [20] K. Sokolowski-Tinten and D. von der Linde. Generation of dense electron-hole plasmas in silicon. *Phys. Rev. B*, 61:2643–2650, Jan 2000.
- [21] Spectra Physics inc. *Manual of the Hurricane Laser*.
- [22] Hao Zhang. *Single-shot femtosecond laser ablation on the nanoscale*. PhD thesis, 2013.
- [23] Hao Zhang, D. van Oosten, D. M. Krol, and J. I. Dijkhuis. Saturation effects in femtosecond laser ablation of silicon-on-insulator. *Applied Physics Letters*, 99(23):231108, 2011.